Chinese Chemical Letters 37 (2026) 111084

Contents lists available at ScienceDirect

Chinese Chemical Letters

journal homepage: www.elsevier.com/locate/cclet

# Multifunctional heterostructure $CoS_2/FeS_2$ catalysts for enhancing high-performance lithium–sulfurized polyacrylonitrile batteries through intrinsic electric fields

Hao Liu[a,b,c,d], Qiang Xu[a,b,c,d], Yun Zhang[a,b,c,d], Na Han[a,b,c,d], Haihui Liu[a,b,c,d,*], Xingxiang Zhang[a,b,c,d,*]

[a] School of Material Science and Engineering, Tiangong University, Tianjin 300387, China
[b] State Key Laboratory of Advanced Separation Membrane Materials, Tianjin 300387, China
[c] Municipal Key Laboratory of Advanced Fiber and Energy Storage, Tianjin 300387, China
[d] Industrial Technology Research Institute of Membranes, Cangzhou Institute of Tiangong University, Cangzhou 061000, China

ARTICLE INFO

*Article history:*
Received 13 January 2025
Revised 7 March 2025
Accepted 12 March 2025
Available online 13 March 2025

*Keywords:*
Lithium-sulfurized polyacrylonitrile batteries
High active material content
Cathode electrolyte interphase
Heterostructure
Intrinsic electric fields

ABSTRACT

Lithium-sulfurized polyacrylonitrile (Li-SPAN) batteries have attracted attention as a unique subset of lithium-sulfur batteries owing to their effectiveness in mitigating the shuttle effect caused by the dissolution of polysulfides. However, traditional SPAN electrodes typically exhibit an active material loading capacity of <40 wt% and demonstrate suboptimal reaction kinetics, which limits their actual performance. In this study, a composite film ($CoS_2/FeS_2$@SeSPAN/CNTs) was developed, which is poised to serve as the cathode in commercial Li-SPAN batteries. The film was fabricated by forming a PAN framework through casting, subsequently growing Fe-ZIF-67 on it *via* hydrothermal processing, and converting it into $CoS_2/FeS_2$ heterostructure and SeSPAN through heat treatment. The porous structure of this material provided numerous sites for active material storage. This effect led to an active material loading capacity of 61 wt%. Experimental results and density functional theory simulations indicated that, owing to the shielding effect of the cathode solid electrolyte interface, the additionally stored active material exhibited an extended all-solid-state reaction mechanism. Furthermore, the internal electric field generated by the $CoS_2/FeS_2$ heterostructure effectively enhanced the adsorption and catalytic conversion of solid polysulfides, thereby improving lithium-ion migration efficiency. As a result, the active material stored in dual-mode exhibited high utilization rates. At a current density of 1 C, the capacity retention of the $CoS_2/FeS_2$@SeSPAN/CNTs cathode was 97.9 % after 800 cycles. This result demonstrated that the design and development of the $CoS_2/FeS_2$@SeSPAN/CNTs composite film significantly enhanced the electrochemical performance of Li-SPAN batteries while paving the way for the commercial exploration of other heterostructural materials in energy storage systems.

© 2026 Published by Elsevier B.V. on behalf of Chinese Chemical Society and Institute of Materia Medica, Chinese Academy of Medical Sciences.

Lithium-sulfur (Li-S) batteries offer unique advantages, which include an energy density six times greater than that of current commercial lithium-ion batteries and low production cost owing to the abundance of sulfur resources [1,2]. Furthermore, the equipment for Li-S battery production is similar to that used for lithium-ion battery production. This condition offers a distinct competitive advantage to Li-S battery manufacturers in the secondary battery market [3,4]. The superior energy density and substantial commercial potential of Li-S batteries have attracted widespread attention in recent years [5]. However, several inherent flaws hinder their commercialization. These flaws include the low electrical conductivity of sulfur, which increases internal resistance and impedes reaction kinetics, and the shuttle effect due to polysulfide dissolution, which reduces sulfur utilization efficiency [6,7].

A common strategy for resolving these flaws involves compositing sulfur with carbon materials to improve conductivity and incorporating polar metallic components to enhance adsorption and catalytic activity. This strategy mitigates the shuttle effect and accelerates electrochemical reaction kinetics [8–12]. However, these methods do not fully resolve the dissolution and shuttling effect of polysulfides. Wang *et al.* altered the dissolution–

* Corresponding authors at: School of Material Science and Engineering, Tiangong University, Tianjin 300387, China.
*E-mail addresses:* liuhaihui@tiangong.edu.cn (H. Liu), zhangpolyu@aliyun.com (X. Zhang).

https://doi.org/10.1016/j.cclet.2025.111084
1001-8417/© 2026 Published by Elsevier B.V. on behalf of Chinese Chemical Society and Institute of Materia Medica, Chinese Academy of Medical Sciences.

precipitation mechanism by covalently bonding sulfur to the main chain of polyacrylonitrile (PAN) to form sulfurized polyacrylonitrile (SPAN). This modification effectively prevents polysulfide formation and significantly improves battery performance [13]. Although SPAN effectively addresses the dissolution and shuttling effects of polysulfides, the scarcity of bonding sites on the PAN molecular chain, along with the need for additional conductive agents, binders, and current collectors, further reduces active material loading capacity [14–16]. Consequently, the actual loading capacity of SPAN rarely exceeds 40 wt% [17]. In our previous work, $SeS_x$ was incorporated into the lotus-root-like pores of SPAN to obtain a standalone cathode with a loading capacity of 53 wt% [18]. During discharge, the insoluble products from the nucleophilic reaction of $SeS_x$ with carbonate electrolytes form a solid electrolyte interface on the surface of the porous structure. This interface protects the extended solid–solid reaction pathway of $S_8$ to $Li_2S$. However, the low conductivity of the solid discharge product, $Li_2S$, exacerbates sulfur accumulation within the battery, which in turn impedes the transfer of electrons and ions to internal sulfur atoms [19–22]. Moreover, high energy barriers prevent the nucleation and decomposition of solid $Li_2S$. This effect impedes the overall reaction kinetics [23]. These challenges become more pronounced as the surface loading of active materials increases. To advance the commercialization of Li-SPAN batteries, it is crucial to develop innovative electrocatalysts that enhance the kinetics of redox reactions. Integrating these electrocatalysts with SPAN cathode materials effectively anchors polysulfides and substantially lowers the reaction barriers for converting $S_8$ to $Li_2S$, thereby accelerating the redox kinetics along this solid-solid reaction pathway. This strategy is expected to improve the efficiency of battery charge-discharge cycles significantly and extend its operational lifespan [24,25]

In this study, a heterostructure with an embedded electric field is proposed. This contraption features graded porous structures and *in situ* encapsulation of the cathode solid electrolyte interface (CEI) to enhance active material loading and improve electrochemical reaction kinetics. A self-supporting SeSPAN film integrated with $FeS_2/CoS_2$ heterostructure nanocages (denoted as $FeS_2/CoS_2$@SeSPAN/CNTs) was synthesized *via* a simple casting method. First, a casting method was employed to create the PAN film. Following this, Fe-ZIF-67 was grown on the PAN framework through a hydrothermal process, and it was subsequently converted into a $CoS_2/FeS_2$@SeSPAN/CNTs *via* heat treatment. This unique structure provides numerous $FeS_2/CoS_2$ heterojunction interfaces, which facilitate electron transfer and increase chemical reactivity. The embedded electric field generated by these heterojunctions further improves reaction kinetics by accelerating the migration of lithium ions and polysulfides across the interface. The well-distributed, uniformly sized $FeS_2/CoS_2$ nanoparticles, characterized by a high specific surface area, act as excellent repositories for active materials and promote the formation of a CEI on their surfaces. The porous nanocage structure effectively mitigates volume expansion, while the externally connected membrane structure reduces electron transport distances, which in turn improves overall reaction kinetics. Consequently, $FeS_2/CoS_2$@SeSPAN/CNTs achieves an active material loading capacity of 61 wt% and delivers an impressive specific capacity of 602 mAh/g over 200 cycles at 0.2 C. Notably, the capacity retention was 97.9 % after 800 cycles at 1 C. Energy level analysis and density functional theory (DFT) calculations provide insights into the influence of the $FeS_2/CoS_2$ heterostructure on polysulfide adsorption and interfacial electron transfer. The heterostructure facilitates the rational design of bimetallic sulfides for SPAN cathodes in Li-SPAN batteries.

The $CoS_2/FeS_2$@SeSPAN/CNTs film with a heterostructure was successfully synthesized *via* a combination of casting, hydrothermal reaction, and heat treatment processes (Fig. 1a). First, PAN was mixed with CNTs to prepare a PAN precursor film with enhanced

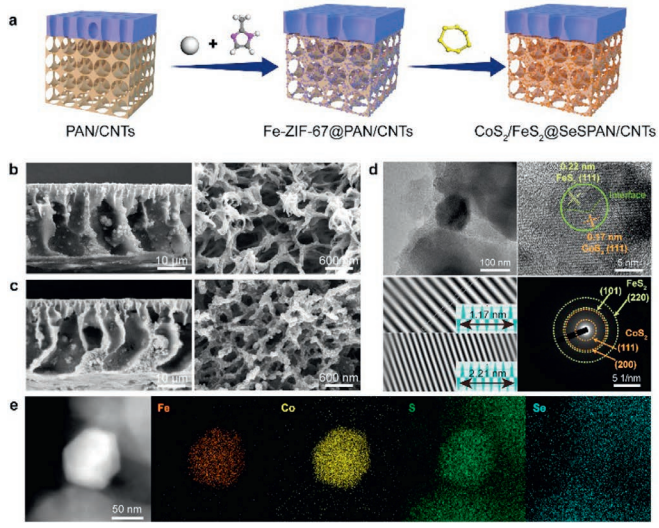



**Fig. 1.** Morphological features: (a) Schematic of the synthesis of $CoS_2/FeS_2$@SeSPAN/CNTs composite film; (b) SEM images of the Fe-ZIF-67@PAN composite film; (c) SEM images of the $CoS_2/FeS_2$@SeSPAN/CNTs composite film; (d) local TEM image of the $CoS_2/FeS_2$@SeSPAN/CNTs composite film, which includes lattice fringe images, lattice spacing details, and diffraction patterns after inverse Fourier transform; and (e) local dark-field image and elemental mapping of the $CoS_2/FeS_2$@SeSPAN/CNTs composite film.

conductivity *via* the casting method. The film (~30 μm thick) formed a structurally intact three-dimensional conductive network (Fig. 1b). Subsequently, the PAN precursor film was immersed in a solution containing 2-Mim, $Fe(NO_3)_3{\cdot}9H_2O$, and $Co(NO_3)_2{\cdot}6H_2O$ for the hydrothermal reaction, which promoted the formation of Fe-ZIF-67 nanoparticles on the film scaffold. Finally, the Fe-ZIF-67@PAN film underwent heat treatment in an argon atmosphere with the addition of $SeS_x$ to form the $CoS_2/FeS_2$@SeSPAN/CNTs film. The binding of selenium with metals is not discussed in detail, as the primary purpose of adding trace amounts of selenium is to utilize the insoluble products formed from the reaction between $SeS_x$ and the electrolyte. These insolubles facilitate the formation of the CEI layer, which prevents direct contact between the electrolyte and the active material [18,26,27]. After heat treatment, the film thickness remained relatively unchanged, and the interconnected network structure remained intact without collapse. $CoS_2/FeS_2$ nanoparticles exhibiting the characteristic rhombic dodecahedral ZIF-67 morphology were observed on the scaffold (Fig. 1c), with particle diameters under 100 nm. Element mapping results confirmed the presence of Co, Fe, and S within the framework (Fig. S1 in Supporting information). High-resolution transmission electron microscopy images revealed the interface between $CoS_2/FeS_2$ nanoparticles and the SeSPAN membrane. This observation indicated strong bonding between the components (Fig. 1d). Distinct crystal and carbon lattice fringes were observed in the $CoS_2/FeS_2$ heterostructure, with lattice fringes corresponding to the (111) crystal planes of $CoS_2$ and $FeS_2$. These planes exhibited interplanar spacings of 0.17 nm and 0.22 nm, respectively. The lattice fringes of $CoS_2$ and $FeS_2$ interweave and extend continuously, indicating a strong coupling between the two materials at the interface, further suggesting the formation of a stable heterostructure. The selected area electron diffraction pattern exhibited diffraction rings corresponding to the (111) and (200) planes of $CoS_2$ and the (101) and (220) planes of $FeS_2$. This result confirmed the excellent crystallinity of the sample. High-angle annular dark-field scanning electron microscopy (HAADF-STEM) and elemental mapping confirmed a uniform distribution of Fe, Co, and S elements. This finding validated the successful preparation of the heterostructure

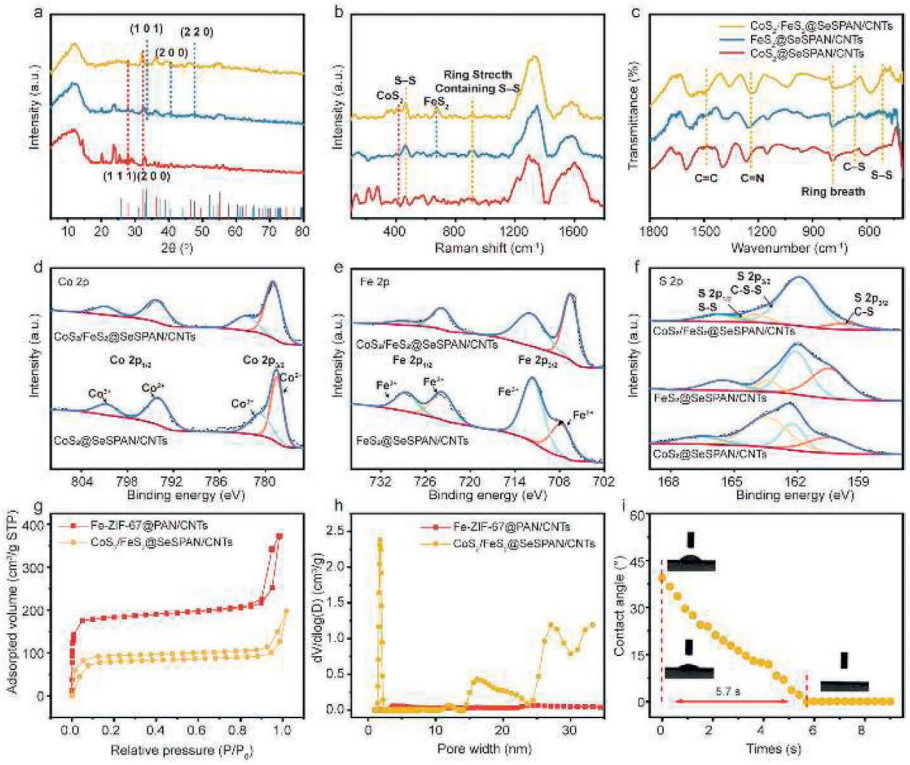



**Fig. 2.** Structural characterization: (a) XRD patterns of $CoS_2$@SeSPAN/CNTs, $FeS_2$@SeSPAN/CNTs, and $CoS_2/FeS_2$@SeSPAN/CNTs. (b) Raman spectra of the composites. (c) FT-IR spectra indicating functional groups in the samples. (d) Co 2p spectra of $CoS_2/FeS_2$@SeSPAN/CNTs. (e) Fe 2p spectra of the composite. (f) S 2p spectra of $CoS_2/FeS_2$@SeSPAN/CNTs. (g) Nitrogen adsorption–desorption isotherms for Fe-ZIF-67@PAN and $CoS_2/FeS_2$@SeSPAN/CNTs. (h) Pore size distribution of the composites. (i) Changes in water contact angle for $CoS_2/FeS_2$@SeSPAN/CNTs during electrolyte wetting.

nanoparticles (Fig. 1e). The complete overlap of these elements indicated a uniform distribution at the interface. The presence of crystalline S and Se elements within the nanoparticles confirmed the incorporation of $SeS_x$. Elemental analysis results revealed that the active material content was up to 61 wt% (Table S1 in Supporting information). Thermogravimetric analysis (TGA) was used to analyze the volatilization of elemental $SeS_x$ between 200 °C and 600 °C, allowing for a rough estimation of the elemental $SeS_x$ loading. The results indicate that the elemental $SeS_x$ loading is highest in $CoS_2/FeS_2$@SeSeSPAN/CNTs, at approximately 23 % (Fig. S2 in Supporting information). The high active material loading capacity demonstrated that the hierarchical porous structure provided ample storage and reaction space for active materials. This condition effectively mitigated volume expansion during the charge-discharge cycles.

X-ray diffraction (XRD) analysis was utilized to characterize the crystalline structure of the samples (Fig. 2a). $CoS_2$@SeSPAN/CNTs and $FeS_2$@SeSPAN/CNTs exhibited characteristic diffraction peaks corresponding to the monometallic sulfides $CoS_2$ and $FeS_2$. This observation confirmed the successful synthesis of the sulfides. The XRD spectrum of $CoS_2/FeS_2$@SeSPAN/CNTs exhibited standard peaks for both $CoS_2$ and $FeS_2$, which included (111) and (200) for $CoS_2$, as well as (101), (200), and (220) for $FeS_2$. This observation provided indirect evidence of the $CoS_2/FeS_2$ heterostructure. Raman spectroscopy (Fig. 2b) and FT-IR spectroscopy (Fig. 2c) further elucidated the composite structure of the $CoS_2/FeS_2$@SeSPAN/CNTs samples. Tables S2 and S3 (Supporting information) present detailed peak information for the $CoS_2/FeS_2$@SeSPAN/CNTs samples. Characteristic peaks corresponding to C–S and S–S bonds indicated that the sulfurization process of PAN and the formation of the six-membered carbon ring framework were unaffected by the incorporation of $CoS_2$ and $FeS_2$.

X-ray photoelectron spectroscopy (XPS) confirmed the presence of Co, Fe, C, S and Se in the $CoS_2/FeS_2$@SeSPAN/CNTs composite (Fig. S3 in Supporting information). Characteristic peaks for pyrrolic and pyridinic nitrogen were observed in the N 1s spectrum. These components enhanced both electron and ion conductivity, which facilitated the adsorption of solid polysulfides. This effect prevented the agglomeration of solid polysulfides encapsulated within the $CoS_2/FeS_2$ dodecahedral structure and maintained the overall reaction kinetics [25,28]. High-resolution Co 2p spectra exhibited peaks at 779.0 eV and 794.3 eV, attributed to $Co^{2+}$, with additional peaks at 782.6 eV and 801.0 eV attributed to $Co^{3+}$ (Fig. 2d). The Co peaks in $CoS_2/FeS_2$@SeSPAN/CNTs exhibited a slight positive shift compared with those in pure $CoS_2$@SeSPAN/CNTs. The shift in the Co 2p peak can be attributed to the formation of the $CoS_2/FeS_2$ heterostructure. In the heterostructure, the interaction between Co and Fe alters the local electronic environment of Co, resulting in a positive shift of the Co 2p peak. This shift typically indicates a change in the electronic density of Co, which is likely due to the stable formation of the $CoS_2$ and $FeS_2$ heterostructure, affecting the electron affinity and lattice strain of Co. This change in electronic density serves as direct evidence for the formation of the heterostructure, highlighting the strong interaction between $CoS_2$ and $FeS_2$ [29]. High-resolution Fe 2p spectroscopy further supports this conclusion (Fig. 2e). The main peaks of Fe $2p_{3/2}$ and Fe $2p_{1/2}$ appear at approximately 710 eV and 724 eV, respectively, indicating that Fe primarily exists in the forms of $Fe^{2+}$ and $Fe^{3+}$. Compared to the pure $FeS_2$@SeSPAN/CNTs sample, the Fe 2p peaks in $CoS_2/FeS_2$@SeSPAN/CNTs shift slightly to higher binding energies, providing further evidence of the interaction between Fe and $CoS_2/FeS_2$, thereby strengthening the indirect evidence for the formation of the heterostructure. In the high-resolution S 2p spectrum, all three samples exhibited S–S, C–S, and C–S–S bonds,

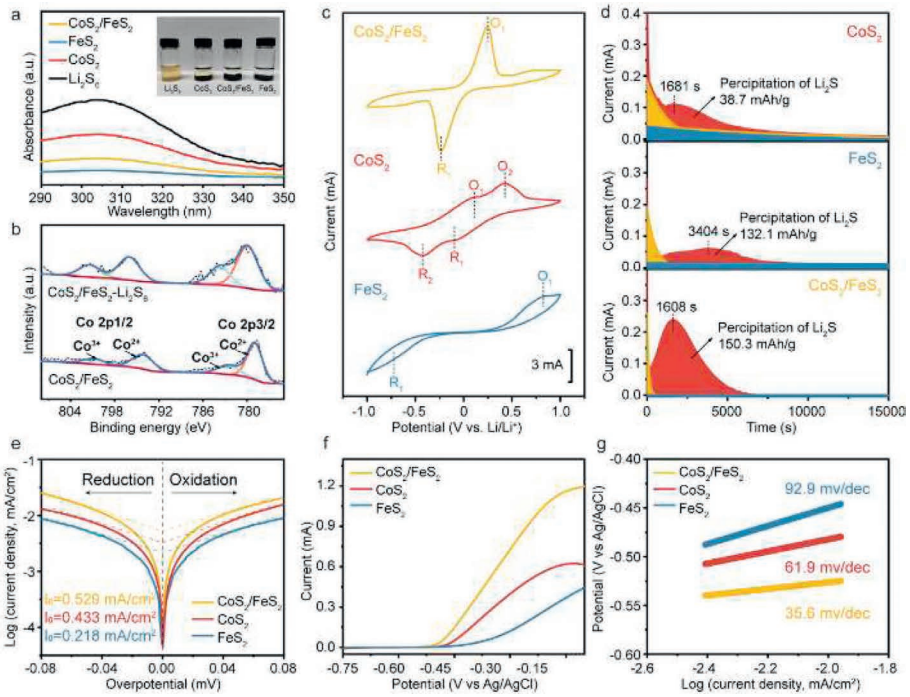



**Fig. 3.** Polysulfide adsorption and electrocatalytic performance: (a) Digital photographs of $Li_2S_6$ solutions after the addition of $CoS_2$, $FeS_2$, and $CoS_2/FeS_2$. (b) Co 2p spectra of $CoS_2/FeS_2$ before and after $Li_2S_6$ adsorption tests. (c) CV curves of symmetric cells with $CoS_2$, $FeS_2$, and $CoS_2/FeS_2$. (d) Deposition behavior of $Li_2S$ on $CoS_2$, $FeS_2$, and $CoS_2/FeS_2$ electrodes. (e) Tafel curves of $CoS_2$, $FeS_2$, and $CoS_2/FeS_2$. (f) LSV curves of $CoS_2$, $FeS_2$, and $CoS_2/FeS_2$ in $Li_2S$ methanol and (g) corresponding Tafel slopes of each material.

while $CoS_2/FeS_2$@SeSPAN/CNTs exhibited a high proportion of C–S–S bonds (Fig. 2f). This observation indicated that the formation of long-chain sulfur within SeSPAN was promoted. The XPS spectra of Se 3d exhibited peaks at 53.9 eV (Se $3d_{5/2}$) and 56.3 eV (Se $3d_{3/2}$), which are characteristic of Se in a covalent $SeS_x$ environment. No low-binding energy peaks, typically associated with metal selenides such as CoSe or FeSe (around 53 eV), were observed. This absence suggests that selenium in the material remains primarily in its covalently bonded $SeS_x$ state, without forming metal selenides with Co or Fe. These findings confirm that Se does not interact with the metal components to form metal selenide phases in the synthesized materials.

Nitrogen adsorption–desorption methods were utilized to assess the surface area and porosity of $CoS_2/FeS_2$@SeSPAN/CNTs films before and after heat treatment (Figs. 2g and h). The Fe-ZIF-67@PAN films initially exhibited a pore volume of 0.062 $cm^3/g$ and a surface area of 20.3 $m^2/g$. After heat treatment at 450 °C, the pore volume of $CoS_2/FeS_2$@SeSPAN/CNTs films increased to 0.306 $cm^3/g$, and the surface area expanded to 43.3 $m^2/g$. The films exhibited a distinct hierarchical porous structure with pore sizes ranging from 2 nm to 30 nm. The films also exhibited notable flexibility and electrolyte wettability, with an electrolyte contact angle of ~40.1° and a wettability time of 5.7 s. These observations highlighted their potential in self-supporting cathode applications for Li-SPAN batteries (Fig. 2i and Fig. S4 in Supporting information).

Performance of $CoS_2/FeS_2$@SeSPAN/CNTs. Enhancing the capacity for polysulfide adsorption at the phase interface is essential for maximizing active material reactivity and increasing electrochemical reaction efficiency. Static adsorption experiments were performed with $Li_2S_6$ solutions to evaluate the polysulfide adsorption capacity of $CoS_2$, $FeS_2$, and $CoS_2/FeS_2$. Optical photographs of the post-experiment samples revealed notable changes in color (Fig. 3a). The solutions containing $FeS_2$ and $CoS_2/FeS_2$ turned colorless within 12 h, while those with only $CoS_2$ exhibited a lighter hue. This observation indicated superior polysulfide adsorption capacity for $CoS_2/FeS_2$. UV–vis absorption spectroscopy confirmed the effective fixation of polysulfides by the $CoS_2/FeS_2$ heterostructure. This suitable fixation effect promoted effective contact and sustained electrochemical reactions. XPS analysis revealed negative shifts in the Co and Fe peaks after the adsorption of $Li_2S_6$. This observation indicated electron acquisition from polysulfide anions through Lewis acid-base interactions (Fig. 3b and Fig. S5 in Supporting information). This finding demonstrated the significant role of the heterostructure in enhancing electrochemical performance by facilitating robust interactions with polysulfides [30,31]. Notably, during the initial reaction stages, the $FeS_2$ component served as the primary binding site for long-chain polysulfides, which subsequently migrated to $CoS_2$ for catalytic conversion. This process enhanced the interaction between $FeS_2$ and $CoS_2$, which in turn facilitated the formation of an electric field that sustained the catalytic processes. To evaluate electrocatalytic activity, CV tests were conducted on $CoS_2$, $FeS_2$, and $CoS_2/FeS_2$ electrodes using $Li_2S_6$ electrolyte (Fig. 3c). The CV tests revealed two pairs of redox peaks in the $CoS_2/FeS_2$ symmetric cell: One pair corresponded to the conversion from $S_8$ to $Li_2S_n$ ($4 \leq n \leq 8$), and the other corresponded to the conversion from $Li_2S_n$ to $Li_2S$ [32]. The $CoS_2/FeS_2$ electrodes exhibited significantly increased current densities in redox reactions, which indicated superior bidirectional catalytic activity due to enhanced electron transfer efficiency and reduced energy barriers. The $Li_2S$ deposition capacity of $CoS_2/FeS_2$ reached 150.3 mAh/g, which was notably higher than that of $CoS_2$ at 38.7 mAh/g and that of $FeS_2$ at 132.1 mAh/g (Fig. 3d). These findings demonstrated the effective combination of the catalytic capabilities of $CoS_2$ with the adsorption capabilities of $FeS_2$ in the heterostructure. Tafel plot tests indicated that $CoS_2/FeS_2$ exhibited the highest exchange current density at 0.501 $mA/cm^2$, which surpassed that of $FeS_2$ at 0.210 $mA/cm^2$ and that of $CoS_2$ at 0.433 $mA/cm^2$. This observation demonstrated the ability of the heterostructure to accelerate charge transfer processes (Fig. 3e). The decomposition and oxidation behavior of $Li_2S$ was evaluated *via* three-electrode lin-

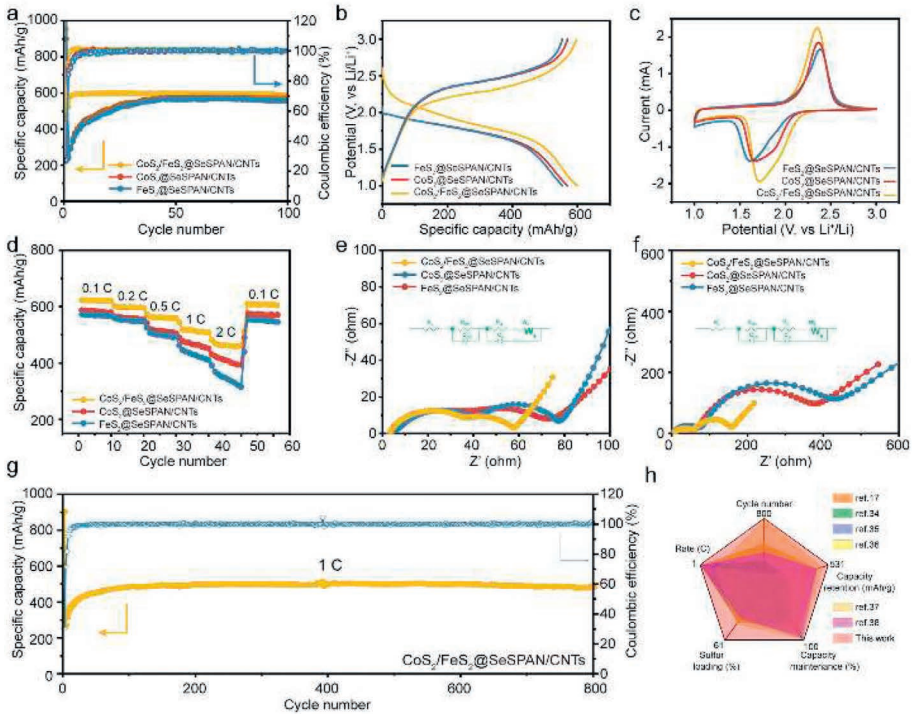



**Fig. 4.** Comprehensive electrochemical evaluation: (a) Cyclic performance of $CoS_2$@SeSPAN/CNTs, $FeS_2$@SeSPAN/CNTs, and $CoS_2/FeS_2$@SeSPAN/CNTs at 0.2 C. (b) Charge–discharge curves for each material. (c) CV curves. (d) Rate capability of $CoS_2$@SeSPAN/CNTs, $FeS_2$@SeSPAN/CNTs, and $CoS_2/FeS_2$@SeSPAN/CNTs at various current densities. (e) Impedance spectra of $CoS_2$@SeSPAN/CNTs, $FeS_2$@SeSPAN/CNTs, and $CoS_2/FeS_2$@SeSPAN/CNTs at fully discharged states after 100 cycles. (f) Impedance spectra at fully charged states after 100 cycles. (g) Long-term cyclic performance of $CoS_2/FeS_2$@SeSPAN/CNTs at 1 C. (h) Comparative electrochemical performance analysis of Li-S batteries with SPAN-based cathodes from this study and previous literature [14,34–38].

ear sweep voltammetry (LSV) using 0.1 mol/L $Li_2S$ in methanol as the electrolyte, along with a platinum counter electrode and an AgCl/Ag reference electrode (Fig. 3f). The $CoS_2/FeS_2$ electrode exhibited a lower onset voltage (−0.51 V) and a stronger current response compared with the $CoS_2$ (−0.49 V) and $FeS_2$ (−0.40 V) electrodes. This observation indicated reduced energy barriers for the conversion of $Li_2S$ to long-chain polysulfides. The Tafel slope for the $CoS_2/FeS_2$ electrode (35.6 mV/dec) was lower than that for the other electrodes, which confirmed the exceptional adsorption and catalytic activity of $CoS_2/FeS_2$ owing to its porous heterostructure (Fig. 3g). This analysis demonstrated the unique capabilities of the heterostructure in enhancing electrochemical performance.

The porous heterostructure of $CoS_2/FeS_2$ functions as a nanoreactor in batteries, which accommodates active materials and facilitates electron transfer. To further investigate $CoS_2/FeS_2$ performance enhancement in SeSPAN cathodes, a series of electrochemical experiments were conducted for comparison with single-component systems. The cycle stability of $CoS_2$@SeSPAN/CNTs, $FeS_2$@SeSPAN/CNTs, and $CoS_2/FeS_2$@SeSPAN/CNTs was evaluated at 0.2 C (Fig. 4a). $CoS_2/FeS_2$@SeSPAN/CNTs achieved a peak stable capacity of 602.3 mAh/g after a brief activation period. The activation behavior is primarily attributed to the interaction between the C and N sites within the SeSPAN framework and lithium ions, leading to the formation of irreversible covalent bonds. These bonds effectively enhance the conductivity of the electrode. The reduced activation cycle time indicates that $CoS_2/FeS_2$@SeSPAN/CNTs offers significant advantages in improving reaction kinetics. In contrast, $CoS_2$@SeSPAN/CNTs and $FeS_2$@SeSPAN/CNTs required ~50 cycles to reach activation. The charge-discharge curves of the electrode after activation indicated notable advantages for $CoS_2/FeS_2$@SeSPAN/CNTs in both capacity and voltage polarization (Fig. 4b). The single discharge plateau observed in the charge–discharge curves and CV curves indicated that the active materials encapsulated within the dodecahedral structure exhibited a solid-solid discharge mode similar to that of SPAN, without generating soluble polysulfides. This observation also indicated the gradual conversion of solid $S_8$ to $Li_2S$ (Fig. 4c). This characterization demonstrated the superior functionality of the $CoS_2/FeS_2$ heterostructure and highlighted its potential in enhancing the electrochemical performance of Li-S batteries. The $CoS_2/FeS_2$@SeSPAN/CNTs electrodes exhibited higher peak current densities and lower polarization compared with the $CoS_2$@SeSPAN/CNTs and $FeS_2$@SeSPAN/CNTs electrodes. The anodic peaks of the electrodes shifted positively to higher potentials, while the cathodic peaks shifted negatively to lower potentials. This finding confirmed enhanced reaction kinetics attributed to the intrinsic electric field and staged catalytic conversion. The Inductively Coupled Plasma (ICP) analysis revealed that the total Fe and Co content in $CoS_2/FeS_2$@SeSPAN/CNTs is 0.9 wt%. In the charge-discharge and CV curves, no significant involvement of $CoS_2$ and $FeS_2$ in lithium-ion insertion/extraction reactions was observed. This indicates that while $CoS_2$ and $FeS_2$ may participate in a small degree of lithium-ion insertion/extraction, their contribution to the overall capacity is minimal. The $CoS_2/FeS_2$ heterostructure primarily enhances the battery performance by facilitating polysulfide conversion and adsorption, rather than directly contributing to the capacity. Rate capability tests (Fig. 4d and Fig. S6 in Supporting information) demonstrated the superior charge–discharge performance of $CoS_2/FeS_2$@SeSPAN/CNTs across various rates, particularly excelling from 0.1 C to 2 C with high recovery rates. Compared with $CoS_2$@SeSPAN/CNTs and $FeS_2$@SeSPAN/CNTs, $CoS_2/FeS_2$@SeSPAN/CNTs exhibited more stable capacities and less capacity fade during high-rate tests. The electrochemical impedance spectroscopy (EIS) results show that the initial electrode impedance is characterized by a curve that does not form a complete semicircle, indicating poor charge transfer resistance

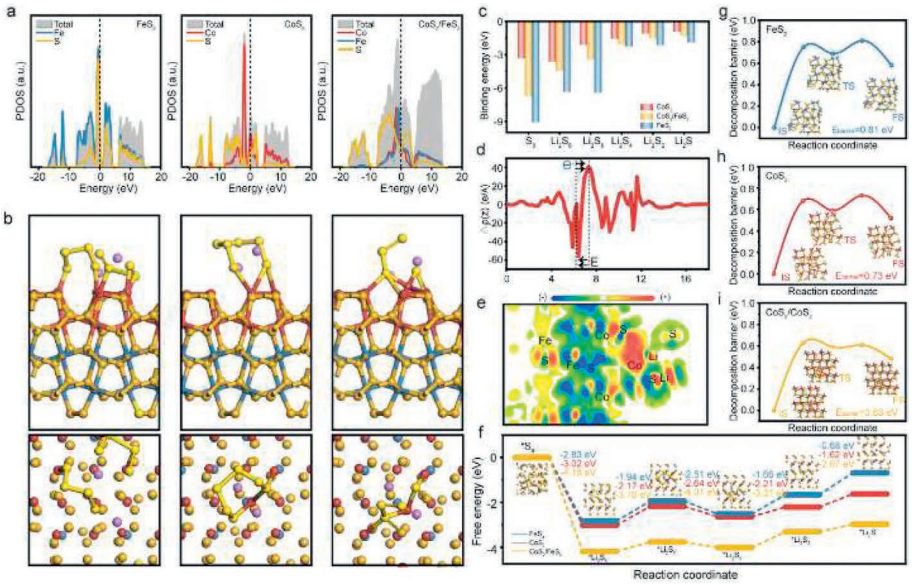


**Fig. 5.** Detailed analysis of cathode electrochemical and physical properties: (a) Calculated PDOS near the Fermi level for $CoS_2$, $FeS_2$, and $CoS_2/FeS_2$. (b) Optimized configurations of $Li_2S_8$, $Li_2S_6$, and $Li_2S_4$ on the surface of $CoS_2/FeS_2$. (c) Adsorption energies between polysulfides and catalysts. (d) Charge accumulation and dissipation per Å in the cross-section after adsorption on $CoS_2/FeS_2$. (e) Corresponding differential charge density map. (f) Gibbs free energy profiles on the surfaces of $CoS_2$, $FeS_2$, and $CoS_2/FeS_2$. (g–i) Decomposition energy barriers for $Li_2S$ on the surfaces of $CoS_2$, $FeS_2$, and $CoS_2/FeS_2$.

($R_{ct}$) in the initial stage (Fig. S7 in Supporting information) [17,18]. After 100 charge-discharge cycles, EIS of each electrode curve exhibited a complete semicircle corresponding to $R_{ct}$ and CEI layer resistance ($R_{CEI}$), confirming that the slow, irreversible insertion of $Li^+$ into the C and N sites of the SPAN framework improves conductivity, thereby reducing $R_{ct}$ (Figs. 4e and f). Additionally, the CEI layer remains stable during cycling. EIS analysis and equivalent circuit fitting results indicate that the $CoS_2/FeS_2$@SeSPAN/CNTs electrode demonstrates the lowest $R_{ct}$ and $R_{CEI}$, highlighting its excellent electrochemical performance (Table S4 in Supporting information). Furthermore, the $R_{ct}$ at 1.0 V during discharge (20 Ω) is lower than at 3.0 V during charge (53 Ω), which is closely related to the interconversion between $Li_2S$ and elemental sulfur or SeSPAN, as well as the formation and rupture of covalent bonds between $Li^+$ and the SeSPAN framework. Long-term cyclic stability assessment is crucial for confirming side reactions in Li-SPAN batteries. Cyclic performance tests were conducted on $CoS_2/FeS_2$@SeSPAN/CNTs at 1 C to investigate whether the electrolyte reacted nucleophilically with sulfur molecules or formed soluble polysulfides under high current density (Fig. 4g). At 1 C, the $CoS_2/FeS_2$@SeSPAN/CNTs electrodes maintained a capacity retention rate of 97.9 % after 800 cycles, with only a 0.003 % capacity fade per cycle and a coulombic efficiency near 100 %. The stable cycling curves indicated that the CEI layer effectively prevented direct contact between the carbonate electrolyte and the sulfur molecules encapsulated within the $CoS_2/FeS_2$ structure to avoid performance degradation due to nucleophilic reactions. The significant capacity reduction observed in the second cycle was attributed to the formation of the CEI layer and the irreversible lithiation of carbon and nitrogen within SeSPAN [19,33]. These observations indicated that the Li-SPAN battery, supported by an intrinsic electric field and enhanced adsorptive catalytic actions, exhibited superior active material loading and electrochemical performance, as well as exceptional redox kinetics compared with the batteries from previous studies (Fig. 4h, Fig. S8 and Table S5 in Supporting information) [14,17,34–38]. The comprehensive analyses demonstrated the potential of the $CoS_2/FeS_2$ heterostructure in advancing Li-SPAN battery technology.

The exceptional performance of $CoS_2/FeS_2$@SeSPAN/CNTs was further investigated *via* DFT calculations to analyze its electronic properties and catalytic capabilities at the atomic level. The configurations of $CoS_2$, $FeS_2$, and $CoS_2/FeS_2$ were examined. Partial density of states (PDOS) analysis revealed no energy gap near the Fermi level. This observation indicated intrinsic conductivity (Fig. 5a). The p-band center of the $CoS_2/FeS_2$ heterostructure was higher (−0.73 eV) than that of $FeS_2$ (−0.80 eV) and $CoS_2$ (−0.97 eV). This observation indicated enhanced interactions with polysulfides. Meanwhile, the D-band center of the $CoS_2/FeS_2$ heterostructure (−1.32 eV) was situated between those of $FeS_2$ (−1.24 eV) and $CoS_2$ (−1.43 eV). This unique electronic configuration indicated optimal electronic properties, which facilitated charge transfer and enhanced catalytic activity for efficient polysulfide conversion. Figs. 5b and c, Figs. S9 and S10 (Supporting information) show the adsorption energies and configurations for various polysulfide intermediates for $CoS_2$, $FeS_2$, and $CoS_2/FeS_2$. $FeS_2$ demonstrated the strongest adsorption energy, while $CoS_2/FeS_2$ exhibited a suitable amount of adsorption energy, which facilitated the desorption of long-chain polysulfides from the substrate. Differential charge density maps indicated a positive correlation between binding energy and electron density. This finding demonstrated the advanced electronic structure of the $CoS_2/FeS_2$ heterostructure (Fig. 5d and Fig. S10). High electron density was observed between Li and S atoms in the transition metal sulfides, where S atoms formed stable covalent bonds with Co and Fe atoms. Cross-sectional charge accumulation diagrams revealed the presence of an intrinsic electric field, which facilitated the adsorption of solid polysulfides and the migration of $Li^+$ (Fig. 5e). Gibbs free energy simulations were conducted to explore the conversion from $S_8$ to longer-chain polysulfides ($Li_2S_8$, $Li_2S_6$, $Li_2S_4$) and final products ($Li_2S_2$, $Li_2S$). Fig. 5f shows the optimized configurations of reaction intermediates and their corresponding free energy curves. $CoS_2/FeS_2$ exhibited a high exothermic effect and low positive Gibbs free energy barriers in subsequent endothermic reactions. This observation indicated thermodynamically favorable conditions for predominant solid-state reactions. Figs. 5g-i and Fig. S11 (Supporting information) show the decomposition energy barriers for $Li_2S$ on the surfaces of $CoS_2$ (0.73 eV), $FeS_2$ (0.81 eV), and $CoS_2/FeS_2$ (0.63 eV). The comprehensive comparison of electronic structures, polysulfide adsorption capacities, and energy barriers

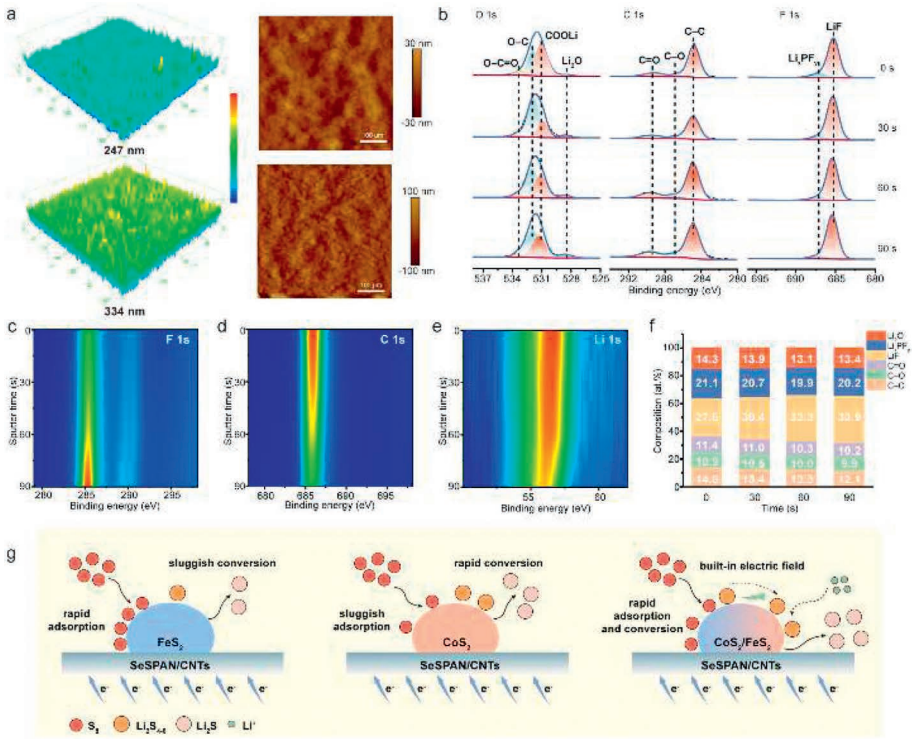



**Fig. 6.** Mechanical and interfacial characterization: (a) Surface roughness comparison of the $CoS_2/FeS_2$@SeSPAN/CNTs cathode before and after 100 cycles. (b) XPS characterization of $CoS_2/FeS_2$@SeSPAN/CNTs with increasing $Ar^+$ sputtering time. Contour maps of (c) F 1s, (d) C 1s, and (e) Li 1s intensity for $CoS_2/FeS_2$@SeSPAN/CNTs under varying sputtering times. (f) corresponding composition content. (g) Schematic of the polysulfide adsorption/conversion processes on $CoS_2$@SeSPAN/CNTs, $FeS_2$@SeSPAN/CNTs, and $CoS_2/FeS_2$@SeSPAN/CNTs.

demonstrated that the $CoS_2/FeS_2$ heterostructure enhanced electronic structure and adsorption capabilities, reduced reaction barriers, and significantly improved electrochemical reaction kinetics. These findings provide theoretical support for the superior electrochemical performance of the $CoS_2/FeS_2$ heterostructure, which demonstrates its advanced capabilities in enhancing Li-SPAN battery technology.

Detailed studies were conducted to comprehensively understand the morphology and chemical composition of the $CoS_2/FeS_2$@SeSPAN/CNTs cathode after extensive cycling. After 100 cycles, the cathode surface exhibited increased roughness and was covered by a thick polymer layer, indicative of the microscopic characteristics of the CEI layer (Fig. S12 in Supporting information). True-color confocal and atomic force microscopy revealed significant contrast variations on the membrane surface, which indicated the formation of a CEI layer ~30 nm thick (Fig. 6a). Further characterization of the surface chemistry of the film *via* XPS etching demonstrated that the outer and sub-surface layers were enriched with C–O and C=O bonds, which was consistent with the decomposition of carbonate electrolytes into organic compounds. Additionally, the XPS spectra indicated the presence of inorganic products, such as $Li_2O$, LiF, and $Li_xPF_y$, resulting from the decomposition of FEC and $LiPF_6$. This observation confirmed the formation of a composite CEI layer consisting of both organic and inorganic materials on the cathode surface (Fig. 6b, Figs. S13 and S14 in Supporting information). Contour maps of C, F, and Li (Figs. 6c-f and Fig. S15 in Supporting information) further indicated that the outer layer of the CEI predominantly comprised carbon-rich organic compounds, while the inner layer predominantly comprised inorganics, mainly LiF and $Li_xPF_y$. Furthermore, the consistent presence of Li and S throughout the etching process confirmed the gradual formation of the CEI layer along the dendritic framework of the SeSPAN membrane, and the CEI layer ultimately covered the entire membrane surface. These findings are in agreement with previous studies, which indicate that the formation of the CEI layer involves electrolyte decomposition, followed by the formation of both organic and inorganic layers, along with nucleophilic reactions between $S^{2-}$ and carbonate electrolytes. When the carbonate electrolyte enters the pores and reacts with $SeS_x$, a nucleophilic reaction occurs, producing insoluble solid products that block the pores and prevent further contact between the electrolyte and $SeS_x$. The inorganic species produced from electrolyte decomposition subsequently nucleate on these products, thereby accelerating the formation of the CEI layer. With the protection of the CEI, the additional $SeS_x$ in the electrode pores can undergo complete charge-discharge cycles, ensuring high utilization of active material. This design not only optimizes the overall battery performance but also ensures the efficient utilization of active materials [26,33].

The porous structure of the $CoS_2/FeS_2$@SeSPAN/CNTs membrane provided numerous attachment sites for active materials. This effect significantly enhanced active material loading capacity. The CEI layer effectively prevented direct contact between the active materials and the electrolyte, which, in turn, prevented the depletion of the additional active materials. Moreover, the enhanced conductivity of the $CoS_2/FeS_2$ heterostructure significantly improves the overall conductivity of the electrode, reducing internal resistance and mitigating early-cycle capacity loss. The intrinsic electric field within the heterostructure facilitates the transport of lithium ions and polysulfides, preventing the formation of dead sulfur and enhancing the utilization of active materials (Fig. 6g). Owing to the synergistic effects of the CEI and the heterostructure, $CoS_2/FeS_2$@SeSPAN/CNTs exhibited exceptional electrochemical performance, which demonstrated its substantial potential in industrial applications.

In conclusion, this study presents a novel flexible $CoS_2/FeS_2$@SeSPAN/CNTs composite film cathode developed

through a combination of straightforward casting technique and hydrothermal reactions. The cathode exhibited remarkable electrochemical performance and substantial potential for industrial applications. The unique graded porous structure of the cathode effectively increased the storage sites for active materials. The cathode achieved a loading capacity of 61 wt%, which significantly exceeded the typical 40 wt% reported in previous studies. Experimental results and DFT calculations indicated that the $CoS_2/FeS_2$ heterointerface significantly enhanced the adsorption and catalytic conversion of polysulfides. The intrinsic electric field at the interface enhanced the migration efficiency of lithium ions. This effect significantly improved the electrochemical reaction kinetics. The synergistic effect of the $CoS_2/FeS_2$ heterojunction, coupled with a protective CEI, significantly facilitated the utilization efficiency of active materials. Notably, even after 800 cycles at 1 C, the battery retained 97.9% of its capacity. This observation demonstrated the exceptional long-cycle performance of the Li-SPAN battery. This work presents a novel solution for the development of high-energy-density, long-cycle-life Li-S batteries, specifically suitable for future high-performance energy storage applications and wearable technologies.

## Declaration of competing interest

Authors declare that they have no known competing financial interests or personal relationships that could have appeared to influence the work reported in this paper.

## CRediT authorship contribution statement

**Hao Liu:** Writing – original draft, Validation, Investigation, Data curation, Conceptualization. **Qiang Xu:** Validation, Investigation, Data curation. **Yun Zhang:** Supervision, Investigation. **Na Han:** Supervision, Investigation. **Haihui Liu:** Writing – review & editing, Investigation, Conceptualization. **Xingxiang Zhang:** Writing – review & editing, Supervision, Investigation, Conceptualization.

## Acknowledgments

This work was supported by the New Materials Research Key Program of Tianjin (No. 18ZXJMTG00110) and the Product Development Fund of Cangzhou Institute (No. TGCYY-Z-0203). We thank the Bianshui Riverside Supercomputing Center (BRSC) for help with the simulation calculations in this manuscript and LetPub (www.letpub.com.cn) for language assistance in the preparation of this manuscript.

## Supplementary materials

Supplementary material associated with this article can be found, in the online version, at doi:10.1016/j.cclet.2025.111084.

## References

[1] G. Zhou, H. Chen, Y. Cui, Nat. Energy 7 (2022) 312–319.
[2] Y. Ding, Z. Sun, J. Wu, et al., J. Energy Chem. 87 (2023) 462–472.
[3] J. Zhou, M.L. Holekevi Chandrappa, et al., Nature 627 (2024) 301–305.
[4] Z. Shi, Y. Ding, Q. Zhang, J. Sun, Adv. Energy Mater. 12 (2022) 2201056.
[5] Y. Li, T. Gao, D. Ni, et al., Adv. Mater. 34 (2022) e2107638.
[6] S. Zhou, J. Shi, S. Liu, et al., Nature 621 (2023) 75–81.
[7] H. Raza, S. Bai, J. Cheng, Electrochem. Energy Rev. 6 (2023) 29.
[8] F. Liang, Y. Zhu, N. Wang, et al., Chin. Chem. Lett. 35 (2024) 109461.
[9] C. Zhao, G.L. Xu, Z. Yu, et al., Nat. Nanotechnol. 16 (2021) 166–173.
[10] Y. Song, M. Zhou, Z. Chen, et al., Chin. Chem. Lett. 35 (2024) 109200.
[11] Z. Huang, P. Jaumaux, S. Bin, et al., Electrochem. Energy Rev. 6 (2023) 21.
[12] Y. Wen, Z. Shen, J. Hui, H. Zhang, Q. Zhu, Adv. Energy Mater. 13 (2023) 2204345.
[13] J. Wang, J. Yang, J. Xie, N. Xu, et al., Adv. Mater. 14 (2002) 963.
[14] A. Abdul Razzaq, G. Chen, X. Zhao, et al., J. Energy Chem. 61 (2021) 170–178.
[15] M.S. Ahmed, S. Lee, M. Agostini, et al., Adv. Sci. 8 (2021) e2101123.
[16] J. Xiang, Z. Guo, Z. Yi, et al., J. Energy Chem. 49 (2020) 161–165.
[17] X. Wang, Y. Qian, L. Wang, et al., Adv. Funct. Mater. 29 (2019) 1902929.
[18] H. Liu, Y. Zhang, Y. Li, et al., Adv. Fiber Mater. 6 (2024) 772–785.
[19] S. Wang, B. Lu, D. Cheng, et al., J. Am. Chem. Soc. 145 (2023) 9624–9633.
[20] W. Hua, H. Li, C. Pei, et al., Adv. Mater. 33 (2021) e2101006.
[21] B. He, Z. Rao, Z. Cheng, et al., Adv. Energy Mater. 11 (2021) 2003690.
[22] Y. Chen, T. Wang, H. Tian, et al., Adv. Mater. 33 (2021) e2003666.
[23] X. Chen, L. Peng, L. Wang, et al., Nat. Commun. 10 (2019) 1021.
[24] S. Xie, X. Chen, L. Wang, et al., eScience 4 (2024) 100222.
[25] Z. Ye, Y. Jiang, L. Li, et al., eScience 3 (2023) 100107.
[26] B. He, D. Liu, Z. Cheng, et al., Adv. Energy Mater. 12 (2021) 2102832.
[27] X. Chen, H. Ji, Z. Rao, et al., Adv. Energy Mater. 12 (2021) 2102774.
[28] B. Yan, Y. Li, L. Gao, et al., Small 18 (2022) e2107727.
[29] H. Xu, Q. Jiang, Z. Shu, et al., Adv. Sci. 11 (2024) e2307995.
[30] K. Wang, Y. Guo, Z. Chen, et al., InfoMat 4 (2021) e12251.
[31] R. Meng, Q. Du, N. Zhong, et al., Adv. Energy Mater. 11 (2021) 2102819.
[32] Y.B. Gao, G.Q. Liu, H.T. Geng, et al., Small 20 (2024) e2312288.
[33] C.D. Qiu, Y. Hu, K. Cao, et al., Adv. Energy Mater. 13 (2023) 2300229.
[34] W. Xue, W. Xu, W. Wang, G. Gao, L. Wang, Compos. Commun. 30 (2022) 101078.
[35] H. Li, W. Xue, L. Wang, T. Liu, ACS Appl. Mater. Interfaces 13 (2021) 25002–25009.
[36] Y. Liu, A.K. Haridas, Y. Lee, K.K. Cho, J.H. Ahn, Appl. Surf. Sci. 472 (2019) 135–142.
[37] A. Abdul Razzaq, Y. Yao, R. Shah, P. Qi, et al., Energy Storage Mater 16 (2019) 194–202.
[38] X. Huang, J. Liu, Z. Huang, et al., Electrochim. Acta 333 (2020) 135493.